ResearchGate

See discussions, stats, and author profiles for this publication at: https://www.researchgate.net/publication/23280508

Ultrasound Elastography: A Dynamic Programming Approach

Article *in* IEEE Transactions on Medical Imaging · November 2008

DOI: 10.1109/TMI.2008.917243 · Source: PubMed

CITATIONS
155

READS
397

6 authors, including:

Emad M. Boctor
Johns Hopkins University
262 PUBLICATIONS **3,344** CITATIONS

SEE PROFILE

Pezhman Foroughi
Johns Hopkins University
32 PUBLICATIONS **624** CITATIONS

SEE PROFILE

Richard Zellars
Johns Hopkins Medicine
47 PUBLICATIONS **1,701** CITATIONS

SEE PROFILE

Gabor Fichtinger
Queen's University
509 PUBLICATIONS **10,675** CITATIONS

SEE PROFILE

All content following this page was uploaded by Pezhman Foroughi on 28 May 2014.

The user has requested enhancement of the downloaded file.

Ultrasound Elastography: A Dynamic Programming Approach

Hassan Rivaz*, Emad Boctor, Pezhman Foroughi, Richard Zellars, Gabor Fichtinger, and Gregory Hager

***Abstract*—This paper introduces a 2-D strain imaging technique based on minimizing a cost function using dynamic programming (DP). The cost function incorporates similarity of echo amplitudes and displacement continuity. Since tissue deformations are smooth, the incorporation of the smoothness into the cost function results in reduced decorrelation noise. As a result, the method generates high-quality strain images of freehand palpation elastography with up to 10% compression, showing that the method is more robust to signal decorrelation (caused by scatterer motion in high axial compression and nonaxial motions of the probe) in comparison to the standard correlation techniques. The method operates in less than 1 s and is thus also potentially suitable for real time elastography.**

***Index Terms*—Dynamic programming, freehand ultrasound (US), real time strain imaging, regularization, ultrasound elastography.**

I. Introduction

ELASTOGRAPHY, the computation of the spatial variation of the elastic modulus of tissue, is an emerging medical imaging method with medical applications such as tumor detection [1]. This paper focuses on static elastography, a well-known technique that applies quasi-static compression of tissue and simultaneously images it with ultrasound. Through analysis of the ultrasound images, a tissue displacement map can be obtained [2], [3]. A least squares technique is then typically used to generate a low noise strain estimate from the displacement map [2].

Despite having numerous potential clinical applications, several practical challenges have hindered wide application of static elastography. First, signal decorrelation between the precompression and postcompression images induces significant noise in the obtained displacement map and is one of the major limiting factors in elastography [4]. Major sources of signal decorrelation are scatterer motion in high axial compression, nonaxial motions of the probe, and physiologic motion. Most elastography techniques estimate local displacements of tissue based on correlation analysis of radio-frequency (RF) echoes [2], [3]. Large windows are required to reduce the variance (i.e., noise) of the estimated displacement and to avoid ambiguity in time delay estimation, especially when tracking a motion that exceeds one wavelength. At the same time, signal decorrelation within large windows limits the tolerable level of compression [2]–[4]. To reduce signal decorrelation, stretching methods have been proposed [5], [6], which are computationally expensive and are not suitable for real-time elastography. Moreover, large errors due to false peaks and smaller errors due to jitter [7] limit the performance of correlation techniques.

Second, in many methods, the compression is applied by a mechanical actuator in order to generate an excitation that minimizes signal decorrelation [1], [8] or because accurate motion is otherwise required by the particular elastography technique [9]. Freehand palpation elastography is a much more attractive alternative, as it requires no extra hardware and provides ease of use. It has attracted increasing interest in recent years [8], [10]–[13], however it introduces additional sources of signal decorrelation caused by operator's hand unwanted motion.

Third, elastography is computationally expensive, making it challenging to display elastograms in real time. Real-time elastography provides the feedback to the operator to best capture the region of interest in the elastogram and is required for image guided surgical operations that can potentially use elastograms. Combined autocorrelation method [14] and phase zero estimation [15] are the first work that generate real-time elastograms. Hall *et al.* [12] have presented a real-time elastography system where tissue compression is performed by freehand palpation based on a 2-D block matching algorithm. Dynamic programming is used for one A-line of the image for guiding the block matching algorithm [16]. While these methods use the displacement of each window to confine the search range for the neighboring windows, the displacement of each window is calculated independently and hence are sensitive to signal decorrelation.

In work closely related to this paper, Pellot-Barakat *et al.* [17] have proposed minimizing an energy function that combines constraints of conservation of echo amplitude and displacement continuity. Since data alone can be insufficient to solve ambiguities due to signal decorrelation, the physical priors of tissue motion continuity increases the robustness of the technique. The RF data is first upsampled by a factor of four in the axial direction. The image is then subdivided into four parts and a coarse displacement map is calculated for each part iteratively. Each part is subsequently divided into four parts and the displace-

Manuscript received December 16, 2007; revised January 3, 2008. First published February 2, 2008; current version published September 24, 2008. This work was supported in part by the National Science Foundation under Grant EEC-9731748 and in part by the Breast Cancer Research Foundation, USA. *Asterisk indicates corresponding author.*

*H. Rivaz is with the Engineering Research Center for Computer Integrated Surgery, Johns Hopkins University, 3400 N. Charles Street, Baltimore, MD 21218 USA.

E. Boctor, P. Foroughi, and G. Hager are with the Engineering Research Center for Computer Integrated Surgery, Johns Hopkins University, Baltimore, MD 21218 USA.

R. Zellars is with the Department of Radiation Oncology, Johns Hopkins University School of Medicine, Baltimore, MD 21231 USA.

G. Fichtinger is with the School of Computing, Queens University, Kingston, ON, K7L 3N6 Canada.

Color versions of one or more of the figures in this paper are available online at http://ieeexplore.ieee.org.

Digital Object Identifier 10.1109/TMI.2008.917243

0278-0062/$20.00 © IEEE

Authorized licensed use limited to: IEEE Xplore. Downloaded on January 5, 2009 at 17:37 from IEEE Xplore. Restrictions apply.

ment of each part is calculated by the same iterative technique using the displacement of the parent grid as an initial guess. The method is shown to generate accurate low noise displacement fields. However, the computation time is reported to be more than 1 min for a strain image that is less than half of the number of pixels in the strain images generated in this paper. Hence, the method is not immediately suitable for real time elastography.

The contribution of this paper is the demonstration of the feasibility of an elastography technique based on dynamic programming (DP) for image matching [18]. Compared to other optimization techniques, DP is an efficient noniterative method of global optimization [19], [20]. However, it can only be used to optimize causal cost functions (Section II).

II. One-Dimensional Displacement Estimation Using DP

Devising a DP algorithm for optimization involves the following.

1) Breaking the total optimization cost into a sum of individual costs, such that each cost corresponds to a discrete decision. The decisions should follow each other sequentially and the cost corresponding to each decision should only depend on the previous and not the future decisions (causality).
2) Determining what decisions are possible at each stage.
3) Writing a recursion on the optimal cost from the first stage to the final stage.

We first consider the problem of 1-D strain estimation with 1-D smoothness regularization. Consider two echo signals $g(i)$ and $g'(i)$ corresponding to two A-lines acquired before and after compression (Fig. 1, left), each signal sampled at $i = 1, 2 \cdots m$. The difference between the two signals Δ can be quantified using sum of absolute differences (SAD), which is computationally inexpensive to compute and has been shown to have good robustness against outliers [21], [20]

$$\Delta(i,d) = |g(i) - g'(i+d)| \tag{1}$$

where $d_{\min} \leq d \leq d_{\max}$ is the displacement at the sample i (Fig. 1, left) and $d_{\min}$ and $d_{\max}$ specify the allowed displacement. Gains of RF data can be changed in ultrasound machines to improve visualization. To reduce the effect of these changes on Δ, both precompression and postcompression ultrasound images are divided by the maximum value of one of the images. The smoothness of the displacements is S

$$S(d_i, d_{i-1}) = (d_i - d_{i-1})^k \tag{2}$$

where d_i is the displacement at the sample i and d_{i-1} is the displacement at the sample $i-1$ of the $g(i)$. To avoid large jumps in the displacement, S should be strictly convex

$$\alpha\,(d_{i1} - d_{i-1})^k + (1-\alpha)\,(d_{i2} - d_{i-1})^k > [\alpha d_{i1} + (1-\alpha) d_{i2} - d_{i-1}]^k\,,\ \ 0 < \alpha < 1 \tag{3}$$

i.e., a small jump and a large jump (left-hand side) are penalized more than two medium jumps (right-hand side). This holds for even k, we choose $k = 2$: for $k > 2$ larger jumps are more heavily penalized which adversely affects contrast to noise ratio.

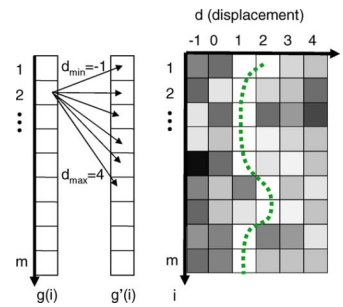

Fig. 1. In the left, values of $g(i)$ and $g'(i+d)$ corresponding to precompression and postcompression RF data are compared. Right shows the cost function C of (4) (white and black represent low and high cost values, respectively).

The cost function C at a point i and associated displacement d_i is defined as a recursive function

$$C(i, d_i) = \min_{d_{i-1}} \{C(i-1, d_{i-1}) + wS(d_i, d_{i-1})\} + \Delta(i, d_i) \tag{4}$$

where w is a regularization weight which governs smoothness. The study of its effect on the estimated displacement is postponed to the discussion of 2-D displacement estimation in Section III-A. The values of the C function are stored in a $(d_{\max} - d_{\min} + 1) \times m$ matrix (Fig. 1, right).

Generally, the optimum value of d_{i-1} should be sought in the entire $[d_{\min},\ d_{\max}]$ range. However, since the strain value is low in elastography, it is expected and desired that at each sample of RF data, the change between the displacement of a sample and its previous sample is not more than 1. Therefore, the search range of optimum value for d_{i-1} is limited to the three values of $d_i - 1$, d_i and $d_i + 1$, which results in a significant gain in speed. ???? This limit on the search range does not affect the results even in a high strain of 10%: Δd is zero for nine samples and one for the tenth sample on average. The value of d_{i-1} that minimizes (4) is also "memoized" [19] in a function M for later use

$$M(i, d_i) = \arg\min_{d_{i-1}} \{C(i-1, d_{i-1}) + wS(d_i, d_{i-1})\}\,. \tag{5}$$

The cost function C is calculated for $i = 1 \cdots m$. The minimum cost at $i = m$ gives the displacement of this point, which is traced back to $i = 1$ using the M function to calculate all the displacements (D)

$$\begin{aligned} D(i) &= \arg\min_{d_i} \{C(i, d_i)\}\,,\ i = m \\ D(i) &= M(i+1, D(i+1)),\ \ i = 1 \cdots m-1. \end{aligned} \tag{6}$$

The displacement map of all A-lines is calculated using the same procedure independently. In Section III, we present a method for coupling adjacent A-lines.

A. Hierarchical Search and Subpixel Displacement Estimation

Further speedup is achieved by downsampling the signal $g(i)$ by a factor of β to $g^*(i)$, and comparing it with the unaltered signal $g'(i)$. This is done by simply skipping $\beta - 1$ samples from $g(i)$ and performing DP on the βth sample, as illustrated in Fig. 2 left. This generates *integer displacement* estimations at m/β samples. The displacement of the skipped samples is then

Authorized licensed use limited to: IEEE Xplore. Downloaded on January 5, 2009 at 17:37 from IEEE Xplore. Restrictions apply.

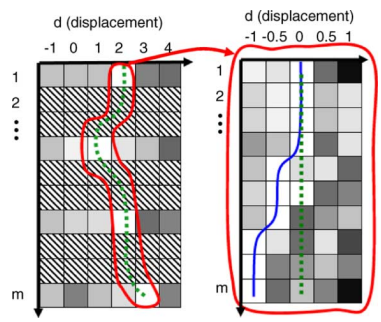

Fig. 2. In the left, the cost function C is shown when DP is performed on $g^*(i)$ ($g(i)$ downsampled by a factor of β) and $g'(i)$ (not downsampled). Hashed squares indicate no cost calculation is performed due to downsampling of $g(i)$, and white and black representing low and high cost values respectively. Displacement is calculated at m/β samples in this stage ($\beta = 3$ in this figure). In right, a new cost function around the optimum path of the first stage's cost function (the dashed line) is created, giving a $1/\gamma = 1/2$ pixel displacement accuracy at m samples.

simply approximated by the linear interpolation of two neighboring points whose displacements are calculated, as an initial guess for the next step.

The displacement estimates are then refined to *subpixel displacement* estimation at all m samples. The original signal $g(i)$ (not downsampled) is compared with $g'(i+d)$ upsampled by a factor of γ (Fig. 2 right) using parabolic interpolation. Repeating the refinement procedure n times results in a refinement factor of $1/\gamma^n$.

???????In cross correlation methods, subsample displacement is usually achieved by interpolation of the correlation function [22], which is subject to bias and jitter [22], [23]. Here, we interpolate the original RF data instead, which is shown to have similar performance [23]. Although cosine-fit outperforms parabolic-fit interpolation in terms of bias and jitter [22], [23], the latter is used here for computational simplicity.

B. Results

For experimental evaluation, RF data was acquired from an Antares Siemens system (Issaquah, WA) with a 7.27-MHz linear array at a sampling rate of 40 MHz. For the purposes of comparison, strain images were also calculated using a standard cross correlation method with a 3-mm window size and 80% overlap and a three point parabolic interpolation to find the subsample location of the correlation peak [22]. Linear regression with a 5-sample window is performed on the displacement field to calculate strain. Normalization was performed to decrease the dynamic range of the strain images: any strain value outside $\bar{s} \pm 3\sigma$ was set to $\bar{s} \pm 3\sigma$ to eliminate the outliers in the strain map ($\bar{s}$ and σ are the mean and standard deviation of the strain values across the whole image). The unitless performance metric signal-to-noise ratio (SNR) and contrast-to-noise ratio (CNR) were calculated according to [2]

$$\mathrm{CNR} = \frac{C}{N} = \sqrt{\frac{2(\bar{s}_b - \bar{s}_t)^2}{\sigma_b^2 + \sigma_t^2}}, \quad \mathrm{SNR} = \frac{\bar{s}}{\sigma} \tag{7}$$

where $\bar{s}_t$ and $\bar{s}_b$ are the spatial strain average of the target and background, σ_t^2 and σ_b^2 are the spatial strain variance of the target and background, and $\bar{s}$ and σ are the spatial average and variance of a window in the strain image, respectively.

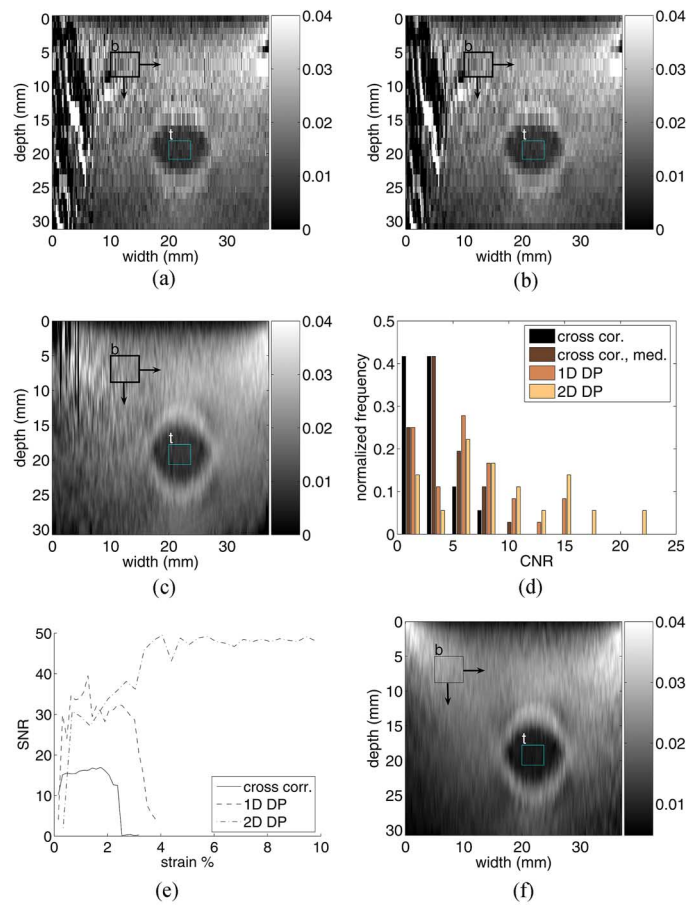

Fig. 3. (a)-(c) strain images obtained from freehand palpation of the phantom using cross correlation, cross correlation with a 3×3 median filter applied on the displacement image and 1-D DP respectively. The target window is fixed on the lesion and the background window is moved to allow multiple CNR calculation. (d) Normalized CNR values of the lesion, obtained by dividing each bin by the total of 36 CNR measurements. (e) SNR values of the cross correlation and 1-D DP techniques. (f) Strain images obtained from freehand palpation of the phantom using 2-D DP.

In the first experiment, a breast elastography phantom (CIRS, Norfolk, VA) with a lesion of 10 mm diameter and three times stiffer than the background was palpated freehand. In consecutive images, where axial compression is low and there is little nonaxial motion, both methods perform well. However, as the axial compression and attendant nonaxial motion increase, the DP method outperforms the cross correlation method. Fig. 3(a) shows the strain image obtained with cross correlation. In Fig. 3(b), a 3×3 median filter is applied to the displacement measurements, before differentiation, as a 2-D continuity check. Fig. 3(c) shows the strain image obtained with the 1-D DP method. A high level of lateral motion, slightly more than 2 A-lines, at the left of the image and high axial strain cause the cross correlation method to fail. To calculate the CNR values the target window was selected as specified in the figure. The background window was then moved across the strain image (with 3.8 mm margin from all four sides and from the lesion where the strain is expected to vary considerably) to allow for a more comprehensive CNR measurement. The histogram of Fig. 3(d) shows that 1-D DP gives better CNR values: the

Authorized licensed use limited to: IEEE Xplore. Downloaded on January 5, 2009 at 17:37 from IEEE Xplore. Restrictions apply.

mean value of the 36 CNR measurements for cross correlation, cross correlation with the 3×3 median filter, and 1-D DP are, respectively, 2.60, 3.98, and 6.24. The standard deviation value of CNR for cross correlation, cross correlation with the 3×3 median filter, and 1-D DP are, respectively, 2.08, 2.70, and 4.27, reflecting the changes in strain across the image caused by medium inhomogeneity and nonuniform loading condition.

To obtain a strain filter [2], a CIRS elasticity QA phantom with the Young's modulus of 33 kPa was compressed in 24 steps, each step 0.005 in. The experiment was performed far from the lesions of the phantom to generate close to uniform strain due to a uniform compression. The strain map between the first frame and all other frame was calculated using the cross correlation and DP methods. The SNR metric was calculated in a small window located at the top center of the image, where strain is approximately constant. Fig. 3(e) shows that the 1-D DP method has a higher dynamic range, an important elastography performance metric [2].

III. 2-D Displacement Estimation

Until now, we have assumed pure axial compression independently estimated on each A-line. However, lateral displacement in a soft material is inevitable even when it undergoes pure axial compression. This displacement is related to the Poisson's ratio, which describes the material compressibility. Also, freehand palpation is rarely a pure compression and thus also results in nonaxial tissue motion. As a result, a 2-D smoothness regularization that considers the displacements between adjacent A-lines is more natural. The DP algorithm of Section II is modified here to allow for 2-D displacement estimation and 2-D smoothness regularization.

Assuming that ultrasound images consist of n A-lines, the distance between the pre and postcompression signals is

$$\Delta(i, j, d_a, d_l) = \left| g_j(i) - g'_{j+d_l}(i + d_a) \right| \tag{8}$$

where $d_{a,\min} \leq d_a \leq d_{a,\max}$ and $d_{l,\min} \leq d_l \leq d_{l,\max}$ are the axial and lateral displacements, respectively, and $j = 1 \cdots n$ refers to jth A-line and $i = 1 \cdots m$

$$S(d_{a_i}, d_{l_i}, d_{a_{i-1}}, d_{l_{i-1}}) = (d_{a_i} - d_{a_{i-1}})^2 + (d_{l_i} - d_{l_{i-1}})^2 \tag{9}$$

is the smoothness regularization with subscripts a and l referring to axial and lateral. The cost function at the ith sample of the jth A-line is

$$C_j(d_a, d_l, i) = \Delta(d_a, d_l, i) + \min_{\delta_a, \delta_l} \left\{ \frac{C_j(\delta_a, \delta_l, i-1) + C_{j-1}(\delta_a, \delta_l, i)}{2} + wS(d_a, d_l, \delta_a, \delta_l) \right\}. \tag{10}$$

For memoization, δ_a and δ_l values that minimize the cost function are stored for all d_a, d_l and i values. The specific form of the cost function allows the calculation of the displacement of each A-line using the cost values of the previous A-line. The cost function of the jth line, $C_j(d_a, d_l, i)$, is calculated and is minimized, resulting in its displacement map. The $C_j(d_a, d_l, i)$ function is also used for the calculation of the next cost function $C_{j+1}(d_a, d_l, i)$ and is deleted from the memory afterward. This makes the amount of memory required to store the cost function values independent of the number of A-lines.

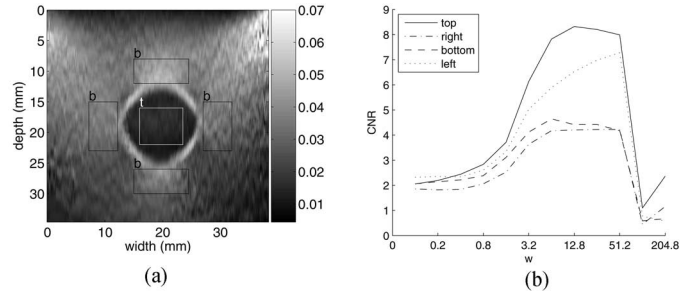

Fig. 4. Two-dimensional DP results of freehand palpation of the breast phantom. (a) Strain image with the target window and four background windows for CNR calculation. (b) CNR values between the target window and the four background windows on the top, right, bottom and left of the lesion calculated for different regularization coefficient values w in (10).

A. Results

To study the effect of the regularization weight w on the CNR, the breast phantom is palpated freehand. For two RF frames, the elastogram is obtained using the 2-D DP algorithm with different w values. CNR is calculated between the shown target window and the four background windows on top, right, bottom, and left of the lesion (Fig. 4). At low w values, CNR is low because of high noise in the windows, while at high w values CNR drops because high displacement changes are heavily penalized. $3 < w < 50$ is optimizing the tradeoff between noise and contrast to maximize CNR, both in the lateral (background windows on the right and left of the target) and axial (background windows on the top and bottom of the target) directions. Since the background windows are close to the lesion, the strain within each window is not expected to be constant even though the phantom is homogeneous within them. This variation in the ground truth strain will be reflected as noise in the CNR calculation which is undesirable. However, we have selected the windows such that they best capture the effect of w on CNR close to an inhomogeneity, which also contains some resolution information.

Fig. 3(f) shows the strain image obtained using the 2-D DP method using the same two frames that are used to generate the strain images in Fig. 3(a)–(c). The CNR values [Fig. 3(d)] are calculated for the same target and 36 background windows as before, giving a mean of 8.96 and a standard deviation of 5.75. Since the elasticity QA phantom cannot be compressed more than 4%, we use the breast phantom for experimental evaluation of the strain filter of the 2-D DP method. Fig. 3(e) shows the SNR values, showing no degradation of the SNR even at a high strain of 10%. Comparing these results with the 1-D DP and cross correlation results, a significant increase in the image quality, CNR value, and maximum allowed strain is achieved.

Substituting other computationally more expensive similarity measures like normalized cross correlation in the Δ function resulted in no significant difference in the performance. Currently, the algorithm takes 0.72 s to calculate the displacement map of each pixel in an image with 1000×100 pixels with maximum

Authorized licensed use limited to: IEEE Xplore. Downloaded on January 5, 2009 at 17:37 from IEEE Xplore. Restrictions apply.

axial displacement of 10 samples (1% strain) and maximum lateral displacement of ± 1 A-lines on a 3.8 GHz P4 CPU. The current implementation is in MATLAB with the DP optimization in mex functions.

IV. Discussion and Conclusion

The lateral search is performed in the 2-D DP method only to decrease the noise and increase the robustness of the axial strain: the lateral displacements are integer values and are not suitable for calculating lateral strain. Results of Fig. 3 show that DP is more robust to the signal decorrelation (caused by scatterer motion in high axial compression, and lateral and out of plane motions of the probe) than standard cross correlation techniques. This is critically important since it tolerates higher axial compression [Fig. 3(e)], increasing the dynamic range of the elastogram which is crucial for lesion detection. Nonlinear elastic properties of tissue also only appear at high strain values [3]. It also generates low-noise elastograms using almost any two frames in freehand palpation, given that they both belong to the same compression or relaxation cycle of the palpation excitation. Finally, no postprocessing step such as median filtering is required.

The CNR and SNR metrics seem to indicate that the regularization creates smooth elastograms while preserving contrast. The only tunable parameter of the method, w in (10), was kept constant at $w = 10$ throughout this work. It can also be varied between 5 and 50, as Fig. 4 indicates, with almost no effect on CNR. This might indicate that the w value optimized for phantom will work well for real tissue. These features of the DP, along with its high speed make it a promising elastography method.

DP strain images in Figs. 3 and 4 show some stress concentration around the lesion which is not seen in the corresponding cross correlation images. We are not sure yet whether this is an artifact or high strains are created just around the lesion because of nonlinear mechanical properties of the phantom. We are planning for validation of the estimated displacement of DP using simulation and laboratory experiments for clarification. High strain is also seen on the top edges in both cross correlation and DP images. The curved shape of the breast phantom is probably the reason for this high strain: in order for the edges of the probe to touch the phantom, the part of the phantom just under middle of the probe has to compress considerably. If the phantom material hardens under high strains, the phantom around the edges experiences higher strain. The absence of this stress concentration in our experiments with noncurved phantoms seems to prove this.

We have chosen to use the cross correlation as a comparative benchmark to assess the potential of DP. This is because cross correlation is the most commonly used method and has been shown to accomplish at least as accurate results as any other method, and thus it represents a "gold-standard" [24], [23]. However, we are planning for a comprehensive comparison of the DP with other strain imaging techniques. Further work is required to study the effect of regularization on resolution [25]. To achieve real-time performance in freehand palpation imaging, an adaptive search range selection can be implemented by using the continuity of displacement in time to confine the search. The 2-D algorithm can be extended to 2-D + t to exploit the cost function in previous time, optimize frame selection [26], and incorporate a 2-D + t regularization.

References

[1] B. Garra, E. Céspedes, J. Ophir, S. Spratt, R. Zuurbier, C. Magnant, and M. Pennanen, "Elastography of breast lesions: Initial clinical results," *Radiology*, vol. 202, pp. 79–86, 1997.

[2] J. Ophir, S. Alam, B. Garra, F. Kallel, E. Konofagou, T. Krouskop, and T. Varghese, "Elastography: Ultrasonic estimation and imaging of the elastic properties of tissues," *Annu. Rev. Biomed. Eng.*, vol. 213, pp. 203–233, Nov. 1999.

[3] J. Greenleaf, M. Fatemi, and M. Insana, "Selected methods for imaging elastic properties of biological tissues," *Annu. Rev. Biomed. Eng.*, vol. 5, pp. 57–78, Apr. 2003.

[4] T. Varghese, J. Ophir, E. Konofagou, F. Kallel, and Righetti, "Tradeoffs in elastographic imaging," *Ultrason. Imag.*, vol. 23, pp. 216–248, 2001.

[5] T. Varghese and J. Ophir, "Enhancement of echo-signal correlation in elastography using temporal stretching," *IEEE Trans. Ultrason. Ferroelectr. Freq. Control*, vol. 44, no. 1, pp. 173–180, Jan. 1997.

[6] P. Chaturvedi, M. Insana, and T. Hall, "2-D companding for noise reduction in strain imaging," *IEEE Trans. Ultrason. Ferroelectr. Freq. Control*, vol. 45, no. 1, pp. 179–191, Jan. 1998.

[7] W. Walker and G. Trahey, "A fundamental limit on delay estimation using partially correlated speckle signals," *IEEE Trans. Ultrason. Ferroelectr. Freq. Control*, vol. 42, no. 2, pp. 301–308, Mar. 1995.

[8] K. Hiltawsky, M. Kruger, C. Starke, L. Heuser, H. Ermert, and A. Jensen, "Freehand ultrasound elastography of breast lesions: Clinical results," *Ultrasound Med. Biol.*, vol. 27, pp. 1461–1469, 2001.

[9] H. Rivaz and R. Rohling, "An active dynamic vibration absorber for a hand-held vibro-elastography probe," *ASME Trans. Vibration Acoustics*, vol. 129, pp. 101–112, Feb. 2007.

[10] M. Doyley, J. Bamber, F. Fuechsel, and N. Bush, "A freehand elastographic imaging approach for clinical breast imaging: System development and performance evaluation," *Ultrasound Med. Biol.*, vol. 27, pp. 1347–1357, 2001.

[11] M. Yamakawa, N. Nitta, T. Shiina, T. Matsumura, S. Tamano, T. Mitake1, and E. Ueno, "High-speed freehand tissue elasticity imaging for breast diagnosis," *Jpn. J. Appl. Phys.*, vol. 42, pp. 3265–3270, May 2003.

[12] T. Hall, Y. Zhu, and C. Spalding, "In vivo real-time freehand palpation imaging," *Ultrasound Med. Biol.*, vol. 29, pp. 427–435, Mar. 2003.

[13] J. Lindop, G. Treece, A. Gee, and R. Prager, "3D elastography using freehand ultrasound," *Ultrasound Med. Biol.*, vol. 32, pp. 529–545, 2006.

[14] T. Shiina, M. Doyley, and J. Bamber, "Strain imaging using combined RF and envelope autocorrelation processing," in *IEEE Ultrason. Symp.*, San Antonio, TX, 1996, pp. 1331–1336.

[15] A. Pesavento, C. Perrey, M. Krueger, and H. Ermert, "A time-efficient and accurate strain estimation concept for ultrasonic elastography using iterative phase zero estimation," *IEEE Trans. Ultrason. Ferroelectr. Freq. Control*, vol. 46, no. 5, pp. 1057–1067, Sep. 1999.

[16] J. Jiang and T. Hall, "A regularized real-time motion tracking algorithm using dynamic programming for ultrasonic strain imaging," in *IEEE Ultrason. Symp.*, Vancouver, BC, Canada, Oct. 2006, pp. 606–609.

[17] C. Pellot-Barakat, F. Frouin, M. Insana, and A. Herment, "Ultrasound elastography based on multiscale estimations of regularized displacement fields," *IEEE Trans. Med. Imag.*, vol. 23, no. 2, pp. 153–163, Feb. 2004.

[18] E. Boctor, G. Fichtinger, G. Hager, and H. Rivaz, "Apparatus and method for computing 3D ultrasound elasticity images," U.S. Patent 26148.071.00us, Jun. 2006.

[19] R. Bellman, *Applied Dynamic Programming*. Princeton, NJ: Princeton Univ. Press, 1962.

[20] M. Brown, D. Burschka, and G. Hager, "Advances in computational stereo," *IEEE Trans. Pattern Anal. Mach. Intell.*, vol. 25, no. 8, pp. 993–1008, Aug. 2003.

[21] P. Huber, *Robust Statistics*. New York: Wiley, 1981.

[22] I. Céspedes, Y. Huang, J. Ophir, and S. Spratt, "Methods for estimation of subsample time delays of digitized echo signals," *Ultrason. Imag.*, vol. 17, pp. 142–171, Apr. 1995.

[23] F. Viola and W. Walker, "A spline-based algorithm for continuous time-delay estimation using sampled data," *IEEE Trans. Ultrason. Ferroelectr. Freq. Control*, vol. 52, no. 1, pp. 80–93, Jan. 2005.

[24] F. Viola and W. Walker, "A comparison of the performance of time-delay estimators in medical ultrasound," *IEEE Trans. Ultrason. Ferroelectr. Freq. Control*, vol. 50, no. 4, pp. 392–401, Apr. 2003.

[25] J. Liu, K. Abbey, and M. Insana, "Linear approach to axial resolution in elasticity imaging," *IEEE Trans. Ultrason. Ferroelectr. Freq. Control*, vol. 51, no. 6, pp. 716–725, Jun. 2004.

[26] M. Lubinski, S. Emelianov, and M. O'Donnell, "Adaptive strain estimation using retrospective processing," *IEEE Trans. Ultrason. Ferroelectr. Freq. Control*, vol. 46, no. 1, pp. 97–107, Jan. 1999.

View publication stats Authorized licensed use limited to: IEEE Xplore. Downloaded on January 5, 2009 at 17:37 from IEEE Xplore. Restrictions apply.